



**HAL**  
open science

# 3D original modelling of phase transformation/mechanics coupling: Effects of internal and external applied stresses on particle growth

Mohamed Gouné, Sylvie Bordère

► **To cite this version:**

Mohamed Gouné, Sylvie Bordère. 3D original modelling of phase transformation/mechanics coupling: Effects of internal and external applied stresses on particle growth. 2019. hal-02187278v1

**HAL Id: hal-02187278**

**<https://hal.science/hal-02187278v1>**

Preprint submitted on 17 Jul 2019 (v1), last revised 17 Sep 2020 (v2)

**HAL** is a multi-disciplinary open access archive for the deposit and dissemination of scientific research documents, whether they are published or not. The documents may come from teaching and research institutions in France or abroad, or from public or private research centers.

L'archive ouverte pluridisciplinaire **HAL**, est destinée au dépôt et à la diffusion de documents scientifiques de niveau recherche, publiés ou non, émanant des établissements d'enseignement et de recherche français ou étrangers, des laboratoires publics ou privés.

# 3D original modelling of phase transformation/mechanics coupling : Effects of internal and external applied stresses on particle growth

S. Bordère<sup>1</sup>, M. Gouné<sup>2</sup>

<sup>1</sup>I2M, Univ. Bordeaux, CNRS, UMR 5295, F-33600 Pessac, France

<sup>2</sup>CNRS, Univ. Bordeaux, Bordeaux INP, ICMCB, UMR 5026, F-33600 Pessac, France

## ABSTRACT

The elastic effects on particle growth were studied from a developed 3D original model that couples explicitly phase transformations and mechanical fields. This model is shown to be able to describe the time-evolution of both chemical and mechanical fields and their interactions in diffusive mass transport. In order to isolate and to analyse some generic effects of elastic fields, the model developed was applied to the growth of an initially single spherical precipitate into a supersaturated matrix in a finite media. We account for both internal and external applied stresses effects on the growth process including both thermo-kinetics and morphological aspects. In all cases studied, the elastic effects are shown to affect the transformation kinetics and equilibrium state. It is also demonstrated that the applied uniaxial compression loading induces an anisotropy of growth that affects both the morphological evolution and hence the equilibrium shape of the particle. This is shown to result to complex interactions between local pressure gradients and local composition gradients.

**KEYWORDS** : precipitation, diffusion, thermodynamics, phase transformation, elastic fields, modelling

## 1. INTRODUCTION

Many of the important properties of metallic alloys such as mechanical properties, conduction and magnetic properties depend on their microstructure feature, i.e. on the volume fraction, the shape and the spatial arrangement of the different phases in the materials [1-4]. The nano/microstructure formation results from phase transformations that are most of the time themselves dependent on complex interactions between different phenomena such as chemical diffusion, interfacial energies and mechanics. In the latter, it is for instance well known that the stresses arising from coherency strain induced by change in crystalline structure, typically due to lattice mismatches, can have a strong influence on the phase diagram [5-8]. Also very important, the internal stresses generated by transformation Eigenstrains are also known to affect the kinetics of phase transformations and both the morphology and the spatial arrangement of phases in the resulting microstructure [9-12]. A typical example is the successive changes of a coherent precipitate while increasing in size during either coarsening or growth in  $\gamma/\gamma'$  Nickel-based superalloys [10, 13]. Indeed, sphere to cube and cube to plate shape transitions were reported together with the so-called “reverse coarsening” corresponding to the splitting of a single cuboidal precipitate into a pair of plates. All of these phenomena were unambiguously related to the existence of internal stresses due to the lattice discrepancy between  $\gamma$  matrix and  $\gamma'$  precipitates. The application of an external stress is also known to affect significantly the microstructure evolution. Indeed, it may influence both the morphology of isolated precipitates and the precipitate coarsening kinetics and destabilize arrays of precipitates resulting in rafted structure [14-17].

The elastic effects on microstructure evolution are however extremely difficult to identify and to quantify from an experimental point of view [7, 8]. That is why, modelling can allow to better understand the interactions between stresses in the general sense of the term and the microstructure evolution in metallic alloys. However, it remains very challenging for many reasons. First, the calculation of both elastic stresses and strains becomes extremely difficult for 3D complex geometries such as in real microstructures [12, 18-20]. Second, the dynamic coupling between diffusive phase transformation and mechanical fields remains a difficult task from a physical point of view [21-23]. Lastly, it requires to track a moving interface with complicated geometry and dynamics and that can develop large singularities and/or topological changes [24]. From numerical point of view, two main different approaches were proposed. The Lagrangian tracking method, in which the interface is explicitly represented by markers. For example, both boundary integral and front tracking methods belong to this type. The Lagrangian method has a long tradition in materials science and dates back more than a century to the work of Stefan [25]. It gives an accurate representation of the interface but is difficult to implement because it requires specific reparametrization and remeshing constantly during the microstructural evolution. This is complicated even further by the topological changes and more especially in three dimensions. The Eulerian capturing method used, for example, in both level set methods and phase field models, offers a good alternative. The interface dynamics is captured by the evolution of a scalar function in an Eulerian framework. It is a suitable method for modelling free boundary problem without having to explicitly track the transformation interface. This presents great advantages for modelling the evolution of complex 3D microstructures [26]. The methodology proposed in this paper is based on the mathematical formulation unifying fluid flow and elastic solid deformation [27, 28]. It rests on a two-step formulation: a lagrangian step and an additional step to determine the eulerian variables from the advection of the lagrangian variables allowing the development of fixed grid methods. An implicit volume method on a staggered grid was chosen for the discretization of the unified equations and the Eulerian Volume of Phase method (VOF) was used to locate the interface [29-31].

In a very recent paper, an accurate description of both stress and strain fields in 3D complex microstructures was obtained from this model [12]. On this basis, we propose to extend it to the diffusive phase transformations which are by nature dynamic. In this case, the interface transformation is mobile and the microstructure evolution is expected to depend on the coupling between mass transport and elastic fields. In this paper, this model is shown to be able to describe the time-evolution of both chemical and mechanical fields and their interactions. In order to isolate and to analyse some generic effects of elastic fields, we consider the problem of the growth of an initially spherical precipitate into a supersaturated matrix in finite media. We account for both internal and external applied stresses effects on the growth process including thermodynamics, kinetics and morphological aspects. In simple cases, our approach is validated from available analytical calculations, using simplifying assumptions.

## 2. GENERAL CONSIDERATIONS

For this purpose, a hypothetic binary A-B was considered. Upon annealing the supersaturated A-B solid solution at a given temperature, precipitation of pure B takes place into the corresponding solid solution. At the initial state, the precipitate has a spherical shape and a given size. For sake of simplicity, both the nucleation step and the effects of interfacial curvature were ignored. Concentrations were measured in terms of mole fraction of component. Superscripts /I and ¥ were used when referring respectively to the interfacial and the far-field matrix

concentrations. A schematic representation of the composition field associated to the hypothetical binary A-B diagram is given in Figure 2.1.

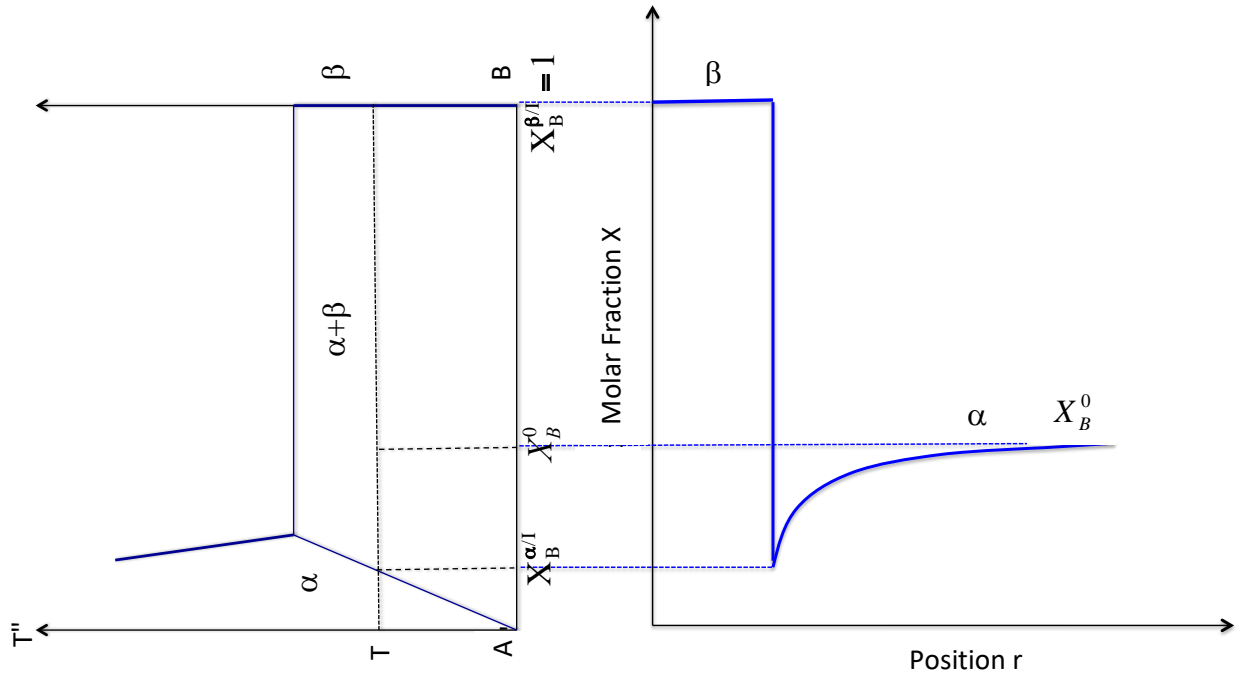


**Figure 2.1** : Schematic representation of the composition field associated to the hypothetical binary A-B diagram

Both the system and the configurations chosen are thus in line with the investigations of the precipitation of pure particle into a binary system.

An extended chemical potential, derived from the theory of solids under stress and that depend on both stress and concentration, is introduced. Its variation follows a Maxwell-type relation, derivable from the expression of Helmholtz free energy [32, 33], and its form is somehow similar to the “diffusion potential” introduced by [34, 35]. The driving force of mass transport is thus associated to the gradient of this extended chemical potential. Contrary to the diffusion flux, the diffusion coefficients are supposed to depend only on temperature and not on both the local composition and stress. It is also worth noting that the solid solution was considered as infinitely dilute and the mechanisms of stress relaxation such as crystal shape optimization and plastic deformation do not occur.

In this paper, the growth of an initially spherical  $\beta$  precipitate into  $\alpha$  parent phase was investigated in three different situations. First, in the absence of elastic effects. Second, in the presence of self-induced elastic field owing to the difference of partial molar volume between precipitate and matrix; the elastic constants for the particle and matrix being identical. This case will be referred as *internal stresses*. Third, a uniaxial compressive loading is applied on the two opposite faces of the cube used for simulation. In that case, the elastic constants were set different for the particle and the matrix in order to induce pressure gradient within the two-phase system.

### 3. 3D MODELLING

In this paper, we present the bases of a new modelling methodology allowing to model diffusional phase changes involving non-isobaric condition that we described in the framework of binary (atoms  $A$  and  $B$ ) and two-phase

(phases  $\alpha$  and  $\beta$ ) compounds. The interface between the two phases is noted  $I$ . The evolving state is described locally at any geometric point  $\mathbf{x}$  of the  $\alpha, \beta$ -phase and time  $t$  with three extensive variables, the temperature  $T(\mathbf{x}, t)$ , the pressure  $p(\mathbf{x}, t)$  and the molar fraction  $X_B(\mathbf{x}, t)$ . Molar concentrations  $C_B(\mathbf{x}, t)$  and  $C_A(\mathbf{x}, t)$ , density  $\rho(\mathbf{x}, t)$ , every thermodynamic coefficient such as the isothermal compressibility coefficient  $\chi_T(\mathbf{x}, t)$  and partial molar volumes  $\bar{V}_B(\mathbf{x}, t)$  and  $\bar{V}_A(\mathbf{x}, t)$  can be defined with these three variables. The condition of local equilibrium at any point  $\mathbf{x}_I$  located on the interface  $I$  corresponds to divariant condition leading to molar fractions  $X_B^{\alpha\text{eq}}(\mathbf{x}_I, t)$  and  $X_B^{\beta\text{eq}}(\mathbf{x}_I, t)$  depending on local pressure  $p(\mathbf{x}_I, t)$  and temperature  $T(\mathbf{x}_I, t)$ . For the final equilibrium state the overall system is divariant and the molar fraction at any point of the system depends on pressure  $p(\mathbf{x})$  and temperature  $T(\mathbf{x})$  only.

For sake of simplicity the indications for the variables of the geometric point  $\mathbf{x}$  and time  $t$  are omitted, as well as the indication of the  $\alpha$  or  $\beta$  phases which is implicit through the location of the  $\mathbf{x}$ -point.

We have first to point out that the diffusion equations are not formulated on the basis of inter-diffusion scheme of the  $A/B$ -couple as it is usually done, but on the basis of the specific diffusion properties of the atoms quantified through the intrinsic diffusion coefficients of A and B. For the present modelling, we consider that precipitation process is limited by diffusion of B. Moreover, no restriction is done about the partial molar volume of A and B which can be highly different from one another, and from a phase to the other. When the partial molar volumes differ from one component to the other, elastic strains develop within the lattice which can relax totally or partially through lattice displacements. The methodology that we propose is based on this concept of the lattice velocity in which diffusion occurs. Hence, the total fluxes of A and B, respectively  $\mathbf{J}_A$  and  $\mathbf{J}_B$ , are defined as follows with  $k = A, B$ .

$$\mathbf{J}_k = \mathbf{J}_{k/D} + C_k \mathbf{V} \quad (1)$$

The subscript  $k/D$  refers to fluxes of the  $k$ -atoms relative to the lattice.

For sake of simplicity,  $\mathbf{J}_{A/D} = \mathbf{0}$  will be considered.  $\mathbf{V}$  is the lattice velocity, also called barycentric velocity since molar fraction  $X_B$  remains constant for this transport;  $C_A$  and  $C_B$  are the concentrations of A and B.

The mass conservation equation for each  $k$ -atom can then be written as follows using total flux equation (1):

$$\frac{\partial C_k}{\partial t} = \Delta \cdot \mathbf{J}_k = \Delta \cdot \mathbf{J}_{k/D} + C_k \Delta \cdot \mathbf{V} \quad (2)$$

Note that, when the partial molar volumes of the components are equal and that for each phase, the total fluxes of the A and B are opposite  $\mathbf{J}_A = -\mathbf{J}_B$ . A unique flux equation (first Fick's law) is necessary in that case to describe such peculiar case without any lattice velocity. It is defined as,

$$\mathbf{J}_B = -\mathbf{J}_A = -D_{A/B} \nabla C_B \quad (3)$$

where the inter-diffusion coefficient  $D_{A/B} = (1 - X_B)D_B + X_B D_A$  is defined using the intrinsic diffusion coefficients and the molar fractions of A and B.

In the general case, where the partial molar partial volumes differ from one another, we have  $\mathbf{J}_A \neq -\mathbf{J}_B$  and non-negligible stresses can remain after the relaxation of the elastic strain energy through the lattice velocity.

These residual stresses can reach values high enough to significantly impact the diffusion process relative to the lattice. Such complex chemical and mechanical coupling cannot be solved in one step from Eq. (2) since: i) the lattice motion  $\mathbf{V}$  driven by diffusion fluxes  $\mathbf{J}_{B/D}$  relative to the lattice involves elastic strain energy relaxation depending on the elastic constants of the  $\alpha, \beta$ -phases, which constitutes a non-trivial mechanical problem and ii) the residual pressure impacts the chemical potential of the diffusive component giving rise to the non-proportionality of the diffusion fluxes to the concentration gradients.

The solving methodology that we propose for such chemical/mechanical coupling during the diffusion process, is based on two sequential solving steps. The first step is dedicated to the solution of diffusion equations at fixed lattice and non-isobaric state. The concentrations, solutions of the diffusion equation at lattice velocity  $\mathbf{V} = 0$ , give rise to a non-equilibrium mechanical state of the system. The aim of the second step is thus to solve the mechanical governing equation in order to obtain the mechanical equilibrium state and to determine the lattice velocity  $\mathbf{V}$  from which all the variables, pressure  $p$ , concentration  $C$ , density  $\rho$ , and molar fraction  $X_B$  of the chemical/mechanical problem can be finally determined.

### 3.1. Diffusion equations at fixed lattice and non-isobaric condition

The diffusion equation relative to the lattice is defined using Eq. (2) and assuming the condition of lattice velocity  $\mathbf{V} = 0$ .

$$\left. \frac{\partial C_{B/D}}{\partial t} \right|_{\mathbf{V}=0} = \nabla \cdot \mathbf{J}_{B/D} \quad (4)$$

The diffusive flux relative to the lattice are defined through the chemical potential gradient using the following equation.

$$\mathbf{J}_{B/D} = -\frac{D_B C_B}{RT} \nabla \mu_B \quad (5)$$

The chemical/mechanical coupling of the diffusion process is here considered through an extended chemical potential  $\mu_B(T, p, X_B)$  which depends on temperature  $T$ , local pressure  $p$  and molar fraction  $X_B$  of the  $B$ -atom. This extended chemical potential is written as follows,

$$\mu_B(T, p, X_B) = \mu_B^*(T, p^*) + RT \ln \left( X_B(T, p) / X_B^*(T, p^*) \right) + \int_{p^*}^p \bar{V}_B(T, p') dp' \quad (6)$$

where  $p^*$  is the reference pressure,  $\bar{V}_B(T, p')$  the partial molar volume of the  $B$ -atom under local pressure  $p'$ , and  $\mu_B^*(T, p^*)$  the chemical potential for the equilibrium state at the reference pressure  $p^*$ . For binary and two-phase system, and for uniform temperature  $T$  and pressure  $p$  within the two-phase system, only two variables are independent for the equilibrium state. So, considering the reference pressure  $p^*$ , the equilibrium state is characterized by well-defined molar fractions  $X_B^{\alpha*}(T, p^*)$  and  $X_B^{\beta*}(T, p^*)$  giving rise to the equality of the extended potential defined as follows.

$$\mu_B^{\alpha*}(T, p^*, X_B^{\alpha*}) = \mu_B^{\beta*}(T, p^*, X_B^{\beta*}). \quad (7)$$

Moreover, during phase transformation, the condition of local equilibrium at the  $\alpha/\beta$ -interface has to be verified at any point located on the interface and any pressure  $p$  through the equality of the chemical potentials relative to the  $\alpha$  and  $\beta$  phases written as follows:

$$\mu_B^{\alpha/\beta}(T, p, X_B^{\alpha eq}(T, p)) = \mu_B^{\beta/\alpha}(T, p, X_B^{\beta eq}(T, p)), \quad (8)$$

where  $X_B^{\alpha eq}(T, p)$  and  $X_B^{\beta eq}(T, p)$  are the molar fractions relative to the  $\alpha, \beta$ -phases intersecting at any point of the interface and characterizing the local equilibrium. Note that the continuity of the chemical potential of  $B$ -atom through the interface corresponds to a discontinuity of their molar fraction.

Finally, assuming that the partial molar volume  $\bar{V}_B(T, p')$  do not vary noticeably with pressure for condensed matter, the extended governing equation for diffusion relative to the lattice can be written as follows,

$$\left. \frac{\partial C_{B/D}}{\partial t} \right|_{\mathbf{v}=0} = -\nabla \cdot \left( D_B C_B^0(T, p^0) \nabla \ln(X_B^0(T, p^0)/X_B^*(T, p^*)) + \frac{D_B C_B^0 \bar{V}_B(T)}{RT} \nabla p^0 \right), \quad (9)$$

where  $p^0$ ,  $C_B^0(T, p^0)$  and  $X_B^0(T, p^0)$  are the known variables at time  $t^0$ , respectively pressure, concentration and molar fraction of the  $B$ -atom.

For an evolving two-phase system under isothermal condition, the intermediate concentration  $C_{B/D}(T, p_D)$  of the  $k$ -atom at time  $t = t^0 + dt$  under the local intermediate pressure  $p_D$  (when lattice is fixed, any concentration variation induces local pressure variation) can be determined from the concentration  $C_B^0(T, p^0)$  at time  $t^0$  and the concentration derivative defined through Eq. (9). We have:

$$C_{B/D}(T, p_D) = C_B^0(T, p^0) + \left. \frac{\partial C_{B/D}}{\partial t} \right|_{\mathbf{v}=0} dt. \quad (10)$$

The molar fraction  $X_{B/D}(T, p_D)$  of the  $B$ -atom at time  $t$  can be defined from the concentrations of A and B  $C_{A/D}(T, p_D)$  and  $C_{B/D}(T, p_D)$  using the following equation.

$$X_{B/D}(T, p_D) = \frac{C_{B/D}(T, p_D)}{C_{A/D}(T, p_D) + C_{B/D}(T, p_D)} \quad (11)$$

As mentioned above, diffusion mass transport at lattice velocity  $\mathbf{V} = \mathbf{0}$ , induces local pressure variation  $dp_D$  during time interval  $dt$ . This intermediate pressure variation in the solving scheme can be calculated from the variation of molar fraction  $dX_{B/D} = X_{B/D}(T, p_D) - X_B^0(T, p^0)$ , partial molar volume  $\bar{V}_B(T)$  and isothermal compressibility coefficient  $\chi_T$ . It gives,

$$dp_D = \frac{1}{\chi_T} \cdot \frac{dX_{B/D} \bar{V}_B(T)}{(1 - X_B^0(T, p^0)) \bar{V}_A(T) + X_B^0(T, p^0) \bar{V}_B(T)}. \quad (12)$$

The intermediate pressure at time  $t$  can then be calculated as,

$$p_D = p^0 + dp_D. \quad (13)$$

This first step in the solving procedure induces non-equilibrium mechanical state. The solving methodology for obtaining the mechanical equilibrium state and allowing the determination of the lattice velocity  $\mathbf{V}$  is described just below.

### 3.2. Second step for lattice velocity solving

The concentration derivative of  $B$  and  $A$  induced by lattice velocity  $\mathbf{V}$  at constant molar fraction  $X_{B/D}$  is defined as:

$$\left. \frac{\partial C_{k/R}}{\partial t} \right|_{X_{B/D}} = C_{k/D} \nabla \cdot \mathbf{V} \quad \text{with } k = B, A \quad (14)$$

The subscript  $R$  refers to the term relaxation.

The unknown lattice velocity can be calculated from the mechanical governing equation defined below (Eq. (15)) and recently developed for multi-phase systems to achieve a unified equation for compressible viscous flow and elastic deformation [27, 28]. This formulation is defined for isothermal condition and within lagrangian representation (variables defined at material points).

$$\rho_D(T, p_D) \frac{d\mathbf{V}}{dt} = -\nabla \left( p_D - \frac{dt}{\chi_T} \nabla \cdot \mathbf{V} \right) + \nabla \cdot \left( \boldsymbol{\tau}^0 + 2\mu^* \left( \frac{1}{2} (\nabla \mathbf{V} + \nabla^t \mathbf{V}) - \frac{1}{3} \nabla \cdot \mathbf{VI} \right) \right) \quad (15)$$

Here,  $\rho_D(T, p_D)$  is the intermediate local density obtained after the first solving step,  $\boldsymbol{\tau}^0$  the shear stress tensor at time  $t^0$ , and  $\chi_T$  the isothermal compressibility coefficient. The intermediate density can be expressed from the intermediate concentrations of  $A$  and  $B$  and their respective molar mass  $M_B$  and  $M_A$  as follows.

$$\rho_D(T, p_D) = C_{A/D}(T, p_D) M_A + C_{B/D}(T, p_D) M_B \quad (16)$$

The viscous behavior corresponds to  $\mu^* = \mu$  where  $\mu$  is the shear viscosity coefficient and  $\boldsymbol{\tau}^0 = 0$ . The isotropic elastic behavior corresponds to  $\mu^* = \mu_E dt$  where  $\mu_E$  is the first Lamé's coefficient. Here, to achieve the lattice velocity driven by diffusion through strain energy relaxation, it is the elastic behavior which has to be considered for both  $\alpha$  et  $\beta$  phases.

The determination of the lagrangian velocities  $\mathbf{V}$  from Eq. (15) allows the update of the problem variables after the elastic energy relaxation through the following equation system.

$$\begin{cases} p_R = p_D - \frac{dt}{\chi_T} \nabla \cdot \mathbf{V} \\ \rho_R(T, p_R) = \rho_D(T, p_D) e^{-dt \nabla \cdot \mathbf{V}} \\ C_{k/R}(T, p_R) = C_{k/D}(T, p_D) e^{-dt \nabla \cdot \mathbf{V}} \\ X_{B/R}(T, p_R) = X_{B/D}(T, p_D) \\ \boldsymbol{\tau}_R = \boldsymbol{\tau}^0 + 2\mu_E dt \left( \frac{1}{2} (\nabla \mathbf{V} + \nabla^t \mathbf{V}) - \frac{1}{3} \nabla \cdot \mathbf{VI} \right) \end{cases} \quad (17)$$

For an eulerian representation of the model where the variables are defined at geometric point  $\mathbf{x}$ , an additional step is required which consists in the advection of the scalar lagrangian variables from their material derivative.

This advection step was precisely described in previous works [27, 28]. The obtained eulerian variables,  $p_R(\mathbf{x})$

,  $\rho_R(\mathbf{x})$ ,  $C_{B/R}(\mathbf{x})$ ,  $C_{A/R}(\mathbf{x})$ ,  $X_{B/R}(\mathbf{x})$ ,  $\tau_R(\mathbf{x})$  and  $\mathbf{V}_R(\mathbf{x})$  at time  $t = t^0 + dt$  after the two-step solving procedure can be simply defined as  $p$ ,  $\rho$ ,  $C_B$ ,  $C_A$ ,  $X_B$ ,  $\tau$ ,  $\mathbf{V}$ . The thermodynamic properties considered for the two phases (see 1. General consideration) make that the partial molar volumes are defined as

$$\bar{V}_A = \bar{V}_B = \frac{1}{C_A + C_B}.$$

### 3.3. Numerical methodology and discretization

The unified equation (15) was discretized in time and space by an implicit volume method on a staggered grid [27, 28, 36]. Compare to collocated grid, staggered grid is powerful to deal with high-pressure gradients and multi-phase flows [37] and to calculate velocity divergence using adjacent points as well. For 3D solving, an iterative bi-conjugate gradient stabilized BICG-StabII [38], preconditioned under a modified and Incomplete LU method, is implemented. Spatial discretization employs centered schemes. In this paper, Eq. (9) was discretized using the same finite volume scheme.

The location of the phases and interfaces is done using the Eulerian Volume of Phase method (VOF) [29-31], where the phase system is numerically built using a phase function  $C$ . In the case of two-phase system, the  $C$ -function varies within the interval [0, 1]. For precipitation process which is the object of this work, the value of the phase  $C$ -function is 0 in the matrix and 1 in the precipitate (See Figure 3.1). The matrix/precipitate-interface is defined as  $C=0.5$ . Every physical constant  $A$  of the system,  $\mu_E$  (1<sup>st</sup> Lamé coefficient),  $\lambda_E$  (2<sup>nd</sup> Lamé coefficient),  $\chi_T$ ,  $D_B$ ,  $\bar{V}_B(T)$ ,  $\bar{V}_A(T)$ , are defined in relation with the  $C$ -function through the continuous relation  $A = (1-C)A^{(0)} + CA^{(1)}$  (the exponents (0) and (1) are assigned to the matrix and precipitate, respectively).

During the iteration process, the phase function  $C^{n+1}$  at time step  $n+1$  is determined from the advection of the phase function  $C^n$  at time step  $n$  and the eulerian velocity field  $\mathbf{V}^{n+1}$  using the following equation.

$$C^{n+1} = C^n - \Delta t \mathbf{V}^{n+1} \cdot \nabla C^n. \quad (18)$$

A Lax–Wendroff TVD scheme with a Superbee limiter for spatial discretization is used to accurately deal with sharp variations of scalar variables at the interface. Note that the scalar lagrangian variables,  $Y_R = V_i$  ( $i = 1, 3$ ),  $C_{k/R}$  ( $k = A, B$ ),  $X_{B/R}$ ,  $p_R$ ,  $\rho_R$ ,  $\tau_{ij/R}$  ( $i = 1, 3; j = 1, 3$ ) obtained after the resolution of the velocity field (Eq. (15) and subsequent variable update (system equation (17)) are advected for an eulerian description relative to the fixed grid using the same time and space discretization schemes as previously defined for the phase function advection.

Finally, at time step  $n+1$ , the isothermal compressibility coefficient  $\chi_T^{n+1}$ , the elastic constants  $\mu_E^{n+1}$  and  $\lambda_E^{n+1}$ , the diffusion coefficient  $D_B^{n+1}$  are updated from the  $C^{n+1}$  function.

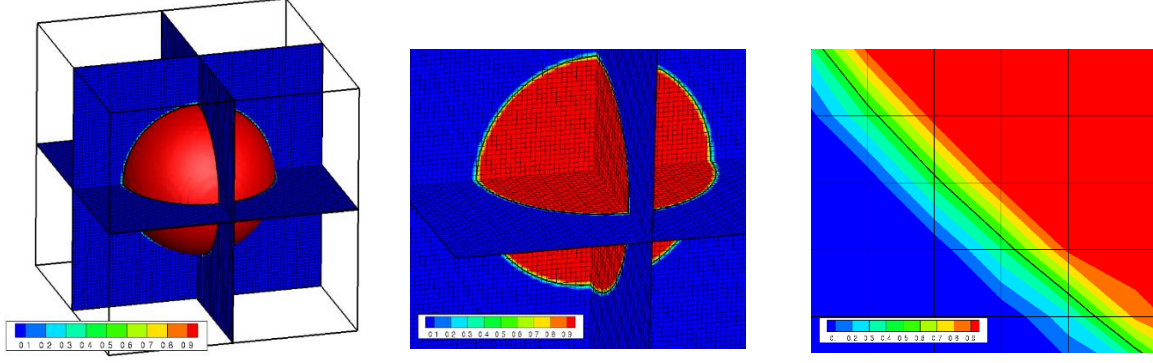


**Figure 3.1** : Visualization of the phase function  $C$  described on a uniform mesh grid. This function allows to discriminate the matrix  $C=0$  (blue color) from the particle  $C=1$  (red color). At the interface, the  $C$ -function varies continuously but sharply within about one element volume. The location of the interface is precisely defined for  $C=0.5$  (full line in black color).

## 4. ANALYTICAL ANALYSIS

### 4.1. Growth rate of a single spherical precipitate into an infinite matrix

Many model on particles growth of various complexities have already been developed. One of the simplest is the well known “Zener model” [39]. It is assumed that particles grow in an infinite media. The growth is then controlled by the long-distance diffusion of atoms and local thermodynamic is assumed at the interface. In binary system, the interface concentration can be easily determined from the thermodynamic phase diagram for the reason that tie-line for transformation depends only on temperature.

Let us suppose that  $\beta$  phase is growing into the supersaturated  $\alpha$  phase. The velocity of such an interface can be calculated using an approximate method due to Zener. The growth rate was determined by approximating the concentration fields around a single precipitate with an analytical solution of the stationary diffusion equation. In that case, the growth rate is given by the following equation:

$$\frac{dR}{dt} = \frac{D_B^\alpha}{R} \left( \frac{X_B^0 - X_B^{\alpha/I}}{X_B^{\beta/I} - X_B^{\alpha/I}} \right) \quad (19)$$

where  $D_B^\alpha = 1$  is the diffusivity of B in the  $\alpha$  matrix,  $X_B^{\alpha/I}$  and  $X_B^{\beta/I}$  are the atomic fractions of B at the  $\alpha/\beta$  interface in matrix and precipitate. In binary system, this value can be determined from the thermodynamic tie-line passing through the nominal composition at a given temperature. It is worth noting that  $X_B^{\beta/I} = 1$  in the present case. The integration of Equation (19) gives the time-evolution of the particle radius as:

$$R(t) = \sqrt{2kD_B^\alpha t + R_0^2} \quad \text{with} \quad k = \left( \frac{X_B^0 - X_B^{\alpha/I}}{X_B^{\beta/I} - X_B^{\alpha/I}} \right) \quad (20)$$

### 4.2. Stress and strain fields associated with a misfitting spherical precipitate

We consider a misfitting  $\beta$ -precipitate of radius  $R$  in a  $\alpha$ -matrix of outer radius  $\lambda$ . The geometry requires to work in a spherical coordinates system defined by the circumferential coordinates  $r$ ,  $\theta$  and  $\varphi$ . We assume a purely elastic and isotropic behaviour for both phases and the  $\alpha/\beta$  interface is supposed to be perfect. Their Young modulus  $E_\alpha$  and  $E_\beta$  and their Poisson coefficients  $\nu_\alpha$  and  $\nu_\beta$  can however be different. For sake of simplicity, the

crystallographic modification associated the  $\alpha \rightarrow \beta$  transformation of a small volume element is expressed by the following Eigenstrain tensor that corresponds to hydrostatic compression or tension:

$$\underline{\underline{\boldsymbol{\varepsilon}^*}} = \begin{pmatrix} \boldsymbol{\varepsilon}^* & 0 & 0 \\ 0 & \boldsymbol{\varepsilon}^* & 0 \\ 0 & 0 & \boldsymbol{\varepsilon}^* \end{pmatrix}$$

where  $\boldsymbol{\varepsilon}^* = \frac{1}{3} \frac{\Delta \bar{V}}{\bar{V}}$ ,  $\Delta \bar{V}$  is the difference between the partial molar volume of matrix and precipitate and  $\bar{V}$  the partial volume of precipitate.

It can be shown, under these simplifying assumptions and by applying both the symmetric boundary condition at  $r=0$  and the free surface condition at  $r=R$ , that [40]:

$$\begin{cases} \sigma_{rr} = \sigma_{\theta\theta} = \sigma_{\varphi\varphi} = \sigma_{\beta} = -K_s (1 - f_v) \boldsymbol{\varepsilon}^* \text{ for } r \leq R \\ \sigma_{rr} = -K_s \left[ \left( \frac{\lambda}{r} \right)^3 - f_v \right] \boldsymbol{\varepsilon}^* \text{ for } r \geq R \\ \sigma_{\theta\theta} = \sigma_{\varphi\varphi} = K_s \left[ \frac{1}{2} \left( \frac{\lambda}{r} \right)^3 - f_v \right] \boldsymbol{\varepsilon}^* \end{cases} \quad (21)$$

Where  $f_v$  is the volume fraction of particle, defined as  $f_v = \left( \frac{R}{\lambda} \right)^3$ .  $K_s$  is defined as follow:

$$K_s = \frac{2}{3} \frac{\frac{E_{\alpha}}{1 - \nu_{\alpha}}}{1 - \left( \frac{\frac{E_{\alpha}}{1 - \nu_{\alpha}}}{\frac{E_{\beta}}{1 - \nu_{\beta}}} \right) (1 - f_v) \left( 1 - \frac{1 + \nu_{\alpha}}{3(1 - \nu_{\alpha})} \right)}$$

It is worth noting that both hydrostatic stresses are uniform in the  $\beta$ -precipitate volume. The level of hydrostatic stress into  $\beta$  is higher since its volume fraction is lower. Furthermore,  $\beta$  is under hydrostatic compression if its molar volume is higher than the one of the  $\alpha$ -matrix.

Into the  $\alpha$ -matrix, the hydrostatic stress is uniform as well. However, the shear stresses are non-uniform since they depend on the distance from the  $\alpha/\beta$  interface. The closer the distance from the  $\alpha/\beta$  interface is, the higher the level of both stresses and strains is.

## 5. SIMULATION RESULTS AND DISCUSSION

### 5.1. Growth of a single spherical precipitate into a matrix in the absence of elastic fields

In this section, the growth of a single spherical precipitate in a matrix in the absence of elastic fields is investigated. The parameters used for calculations are given in Table 1.

**Table 1:** Parameters used for calculations

	Symbol	$\alpha$ -phase	$\beta$ -phase
Initial density (g/cm <sup>3</sup> )	$\rho^i$	7.874	7.874
Equilibrium molar fraction of B at $p^*$	$X_B^*$	0.08	1.0
Initial molar fraction of B at $p^*$	$X_B^i$	0.1	1.0
Molar mass (g)	$M_A = M_B$	55.8	55.8
Initial total molar concentration (mol.cm <sup>-3</sup> )	$C^i$	0.141	0.141
Partial molar volume at $p^*$ (cm <sup>3</sup> /mol)	$\bar{V}_A^* = \bar{V}_B^*$	7.087	7.087
Initial partial molar volume at $p^i$ (cm <sup>3</sup> /mol)	$\bar{V}_A^i = \bar{V}_B^i$	7.087	7.087
Molar temperature energy (J/mol)	$RT$	6842	6842
Temperature (K)	$T$	823	823
Diffusion coefficient of B (m <sup>2</sup> .s <sup>-1</sup> )	$D_B$	$2.5 \times 10^{-10}$	-

The initial configuration for the calculations corresponds to a volume fraction of  $\beta$ -precipitate of 0.052% ( $f_v=0.052\%$ ) and a size defined from the dimensionless number  $\frac{R}{L} = 0.05$ ; where  $L$  is the simulation box length.

The 3D morphology as well as the size change of the  $\beta$ -precipitate at 823K calculated from the “3D model” at both the initial and final time are given in Figure 5.1.

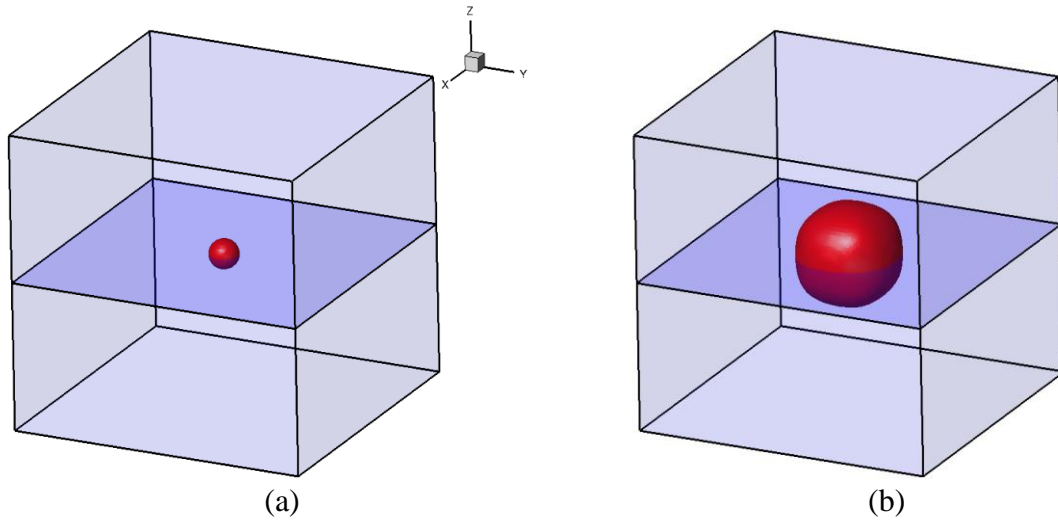


**Figure 5.1 :** 3D-morphology and size change of the particle between (a) starting time ( $t \times D/L^2 = 0$ ) and (b) final time ( $t \times D/L^2 = 1.8$ ) of the growth process.

It is shown that the  $\beta$ -precipitate remains almost spherical throughout the growth process. A slight deformation of the  $\beta$ -precipitate was highlighted for the highest volume fractions. This mainly results from the interactions between the diffusion fields and the free boundaries. As expected, the evolution of the molar fraction of B at different characteristic times of the growth process within the three equivalent planes  $x=0.5$ ,  $y=0.5$  and  $z=0.5$  shows a progressive depletion of B into the matrix (Figure 5.2).

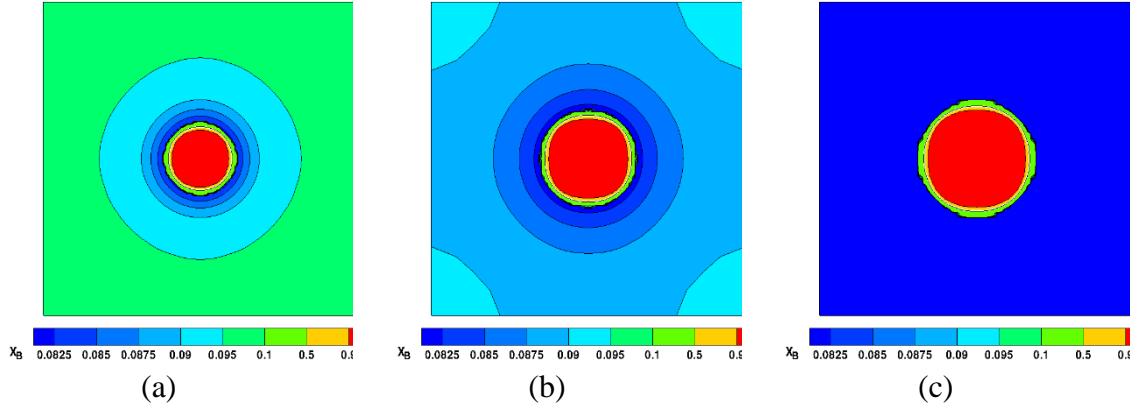


**Figure 5.2** : Molar fractions of B at different characteristic times of the growth process within the three equivalent middle plane  $x=0.5$ ,  $y=0.5$  and  $z=0.5$ . (a)  $t \times D/L^2 = 0.15$ ; (b)  $t \times D/L^2 = 0.4$ ; (c)  $t \times D/L^2 = 1.8$ .

The kinetics of growth is shown to be parabolic at the beginning of transformation and the growth rate corresponds perfectly to that approximated by the Zener model (Figure 5.3).

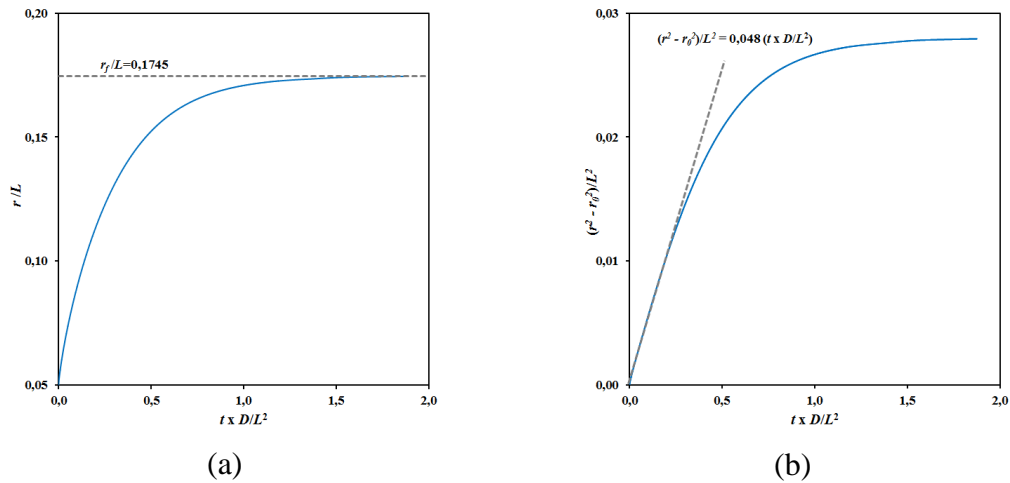


**Figure 5.3** : Growth kinetics of the particle. (a), evolution of the adimensional particle radius  $r/L$ . The dashed line correspond to the equilibrium adimensional radius. (b), evolution of the square of the adimensional particle radius. A linear evolution is highlighted at short time and the corresponding linear coefficient ( $2k = 0.048$ ) is very close to that approximated by Zener ( $2k_{th}=0.044$ ).

For longer time, the growth rate decreases drastically due to the overlapping of the diffusion fields which is not taken into account in the classical Zener approach. The profiles of B calculated close to the  $\alpha/\beta$  interface at different times are given in Figure 5.4. As expected in the binary systems, the molar fraction of B at the interface remains almost constant during the growth process. However, a small deviation to the equilibrium condition at

the  $\alpha/\beta$  interface is observed. It is more visible in the profiles evolution of chemical potential of B in Figure 5.5, where  $\mu_B$  is not strictly equal to zero at the interface. This deviation was mainly attributed to the continuous description of the phase function C at the interface between mesh nodes. The interface being defined by  $C=0.5$ , it is obvious the higher the mesh refinement, the more precise the value of the potential defined at the interface.

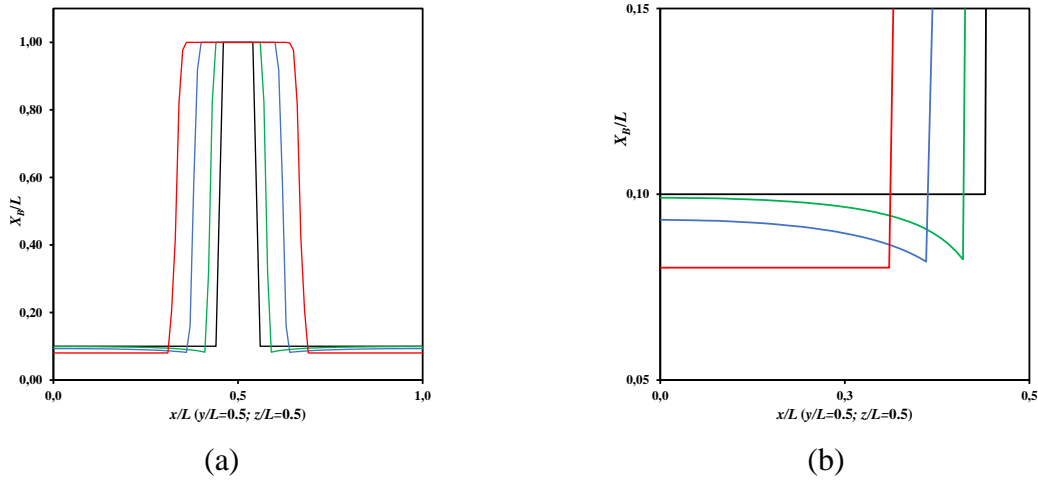


**Figure 5.4 :** Profiles along the three equivalent middle lines  $(x/L, y/L=0.5, z/L=0.5)$ -line,  $(x/L=0.5, y/L, z/L=0.5)$ -line and the  $(x/L=0.5, y/L=0.5, z/L)$ -line of molar fraction of B at different times of the particle growth. (a), the molar fraction jump at the interface. (b), magnification of the profiles close to the transformation interface.

—  $t \times D/L^2 = 0$ ;      —  $t \times D/L^2 = 0.056$   
—  $t \times D/L^2 = 0.26$ ;    —  $t \times D/L^2 = 1.8$

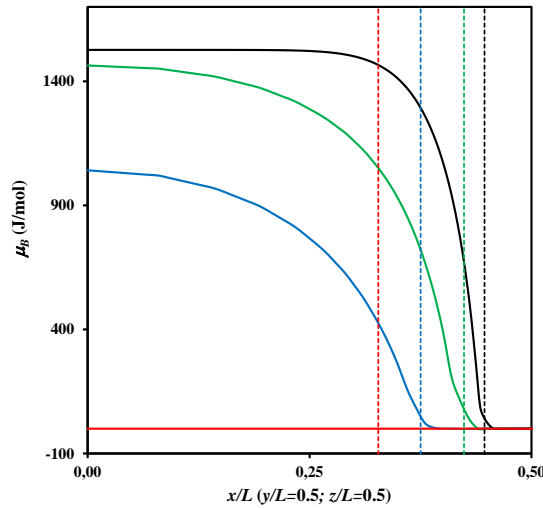


**Figure 5.5 :** Chemical potential profiles of B along the three equivalent middle lines  $(x/L, y/L=0.5, z/L=0.5)$ -line,  $(x/L=0.5, y/L, z/L=0.5)$ -line and the  $(x/L=0.5, y/L=0.5, z/L)$ -line at different times during particle growth. The value of the chemical potential at the interface, which is located through the dashed lines for every evolving times, remains nearly constant and close to zero during growth particle.

—  $t \times D/L^2 = 0.0125$ ;    —  $t \times D/L^2 = 0.056$   
—  $t \times D/L^2 = 0.26$ ;      —  $t \times D/L^2 = 1.8$

## 5. 2. Growth of a single spherical misfitting precipitate into a matrix

In order to examine the effects of elastic field on precipitate growth, we consider the problem of the diffusional growth of a spherical precipitate into a supersaturated matrix having different partial molar volume. The precipitate has thus an associated misfit which is defined with respect to the partial molar volume of both matrix and precipitate. In that case, we account explicitly for elastic fields resulting from transformation on the precipitation process itself through the extended chemical potential (Equation 6). The parameters are given in Table 1 except for the parameters specifically used for this present problem, which are indicated in Table 2.

**Table 2 : Parameters used for calculations**

	Symbol	$\alpha$ -phase	$\beta$ -phase
Young's modulus (GPa)	$E_Y$	210	210
Poisson coefficient (GPa)	$\nu$	0	0
1 <sup>st</sup> Lamé's coefficient (GPa)	$\mu_E$	105	105
2 <sup>nd</sup> Lamé's coefficient (GPa)	$\lambda_E$	0	0
Isothermal compressibility coefficient (Pa <sup>-1</sup> )	$\chi_T$	$1.43 \times 10^{-11}$	$1.43 \times 10^{-11}$
Initial pressure (MPa)	$p^i$	0	83.9
Partial molar volume at $p^*$ (cm <sup>3</sup> /mol)	$\bar{V}_A^* = \bar{V}_B^*$	7.087	7.0955

The 3D calculations show, in Figure 5.6, that both the elastic stress and composition fields are isotropic during the growth process of precipitate. In that case, both the interfacial concentration and the diffusion flux are shown to be uniform at all points along the precipitate-matrix interface and, consequently, the precipitate morphology remains almost spherical.

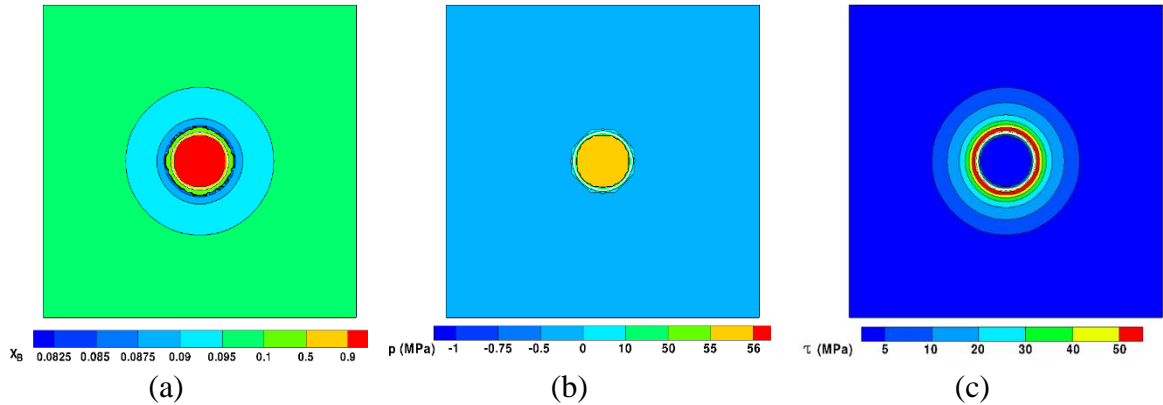


**Figure 5.6 :** Maps within the three equivalent middle plane  $x=0.5$ ,  $y=0.5$  and  $z=0.5$  of (a) molar fraction of B, (b) pressure and (c) normalized shear stress at time  $t \times D/L^2 = 0.15$ .

The evolution of hydrostatic stresses in both precipitate and matrix as a function of the particle radius agrees very well with the analytical results (Equation 21 and Figure 5.7). Overall, the results show that the matrix is in tension while the particle is in compression (Figure 5.7) and the elastic fields are uniform in both matrix and precipitate

(Figure 5.8). These results are in agreement with both the Scherrer's model [40] and the simpler Eshelby model [41].

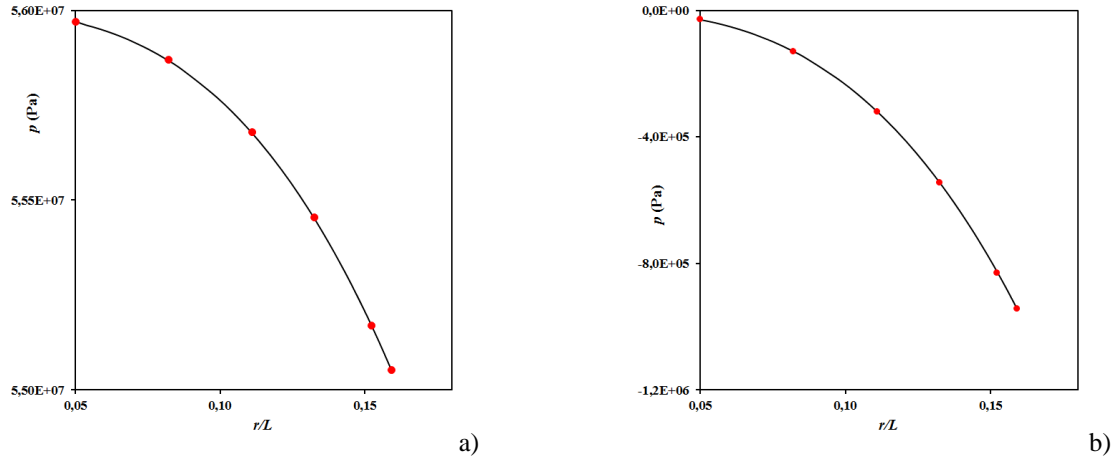


**Figure 5.7** : Evolution of the pressures as a function of the adimensional particle radius  $r/L$  at: (a) the  $(x=0.5, y=0.5, z=0.5)$ -point located in the  $\alpha$ -phase and (b) the  $(x=0.15, y=0.5, z=0.5)$ -point located in the  $\beta$ -phase. This evolution is compared for some volume fractions (red dots) to that obtained analytically from the Scherrer's model [40].

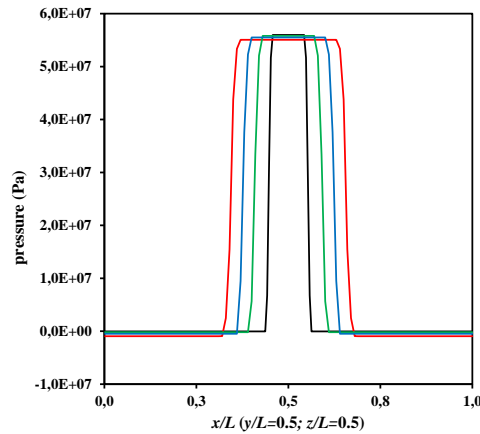


**Figure 5.8**: Pressure profiles along the three equivalent middle lines  $(x/L, y/L=0.5, z/L=0.5)$ -line,  $(x/L=0.5, y/L, z/L=0.5)$ -line and the  $(x/L=0.5, y/L=0.5, z/L)$ -line at different times of the particle growth when transformation induces stress is involved and complete chemical potential with chemical/mechanical coupling is considered.

—  $t \times D/L^2 = 0$ ;      —  $t \times D/L^2 = 0.15$   
—  $t \times D/L^2 = 0.4$ ;      —  $t \times D/L^2 = 1.8$

The calculations given in Figure 5.9 show that the growth kinetics is strongly influenced although the elastic effects do not change the classical  $t^{1/2}$  temporal power law for precipitate growth at the beginning of transformation as already highlighted in [21, 42]. The elastic effects affect both the magnitude of the growth coefficient and the equilibrium radius of the precipitate. As shown by the profiles of composition given in Figure 5.10, the effect of elastic field is to shift the interface composition to the far-field concentration. This tends to decrease the overall growth rate of the precipitate with respect to the unstressed case (see Figure 5.4b).

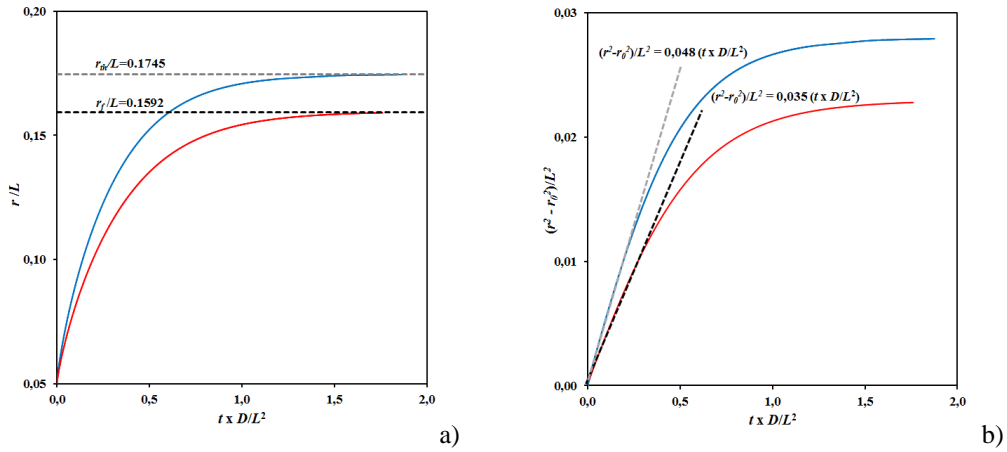


**Figure 5.9 :** Comparison of the particle growth kinetics. The blue curve and the red curve correspond respectively to the unstressed and stressed case. (a), evolution of the adimensional particle radius  $r/L$ . The dashed line correspond the the equilibrium values. (b), evolution of the square of the adimensional particle radius. In both cases, a linear evolution is highlighted at short time and the linear coefficient is smaller in the stressed case (0.035 vs 0.048).

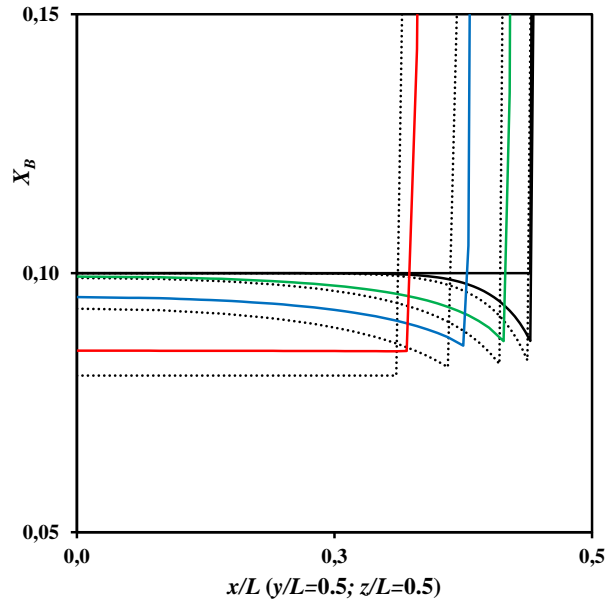


**Figure 5.10 :** Comparison of the concentration profiles of B within the  $\alpha$ -phase along the three equivalent middle lines  $(x/L, y/L=0.5, z/L=0.5)$ -line,  $(x/L=0.5, y/L, z/L=0.5)$ -line and the  $(x/L=0.5, y/L=0.5, z/L)$ -line during the particle growth. The dashed line and the solid line correspond respectively to the unstressed and stressed case.

—  $t x D/L^2 = 0$ ;      —  $t x D/L^2 = 0.056$   
 —  $t x D/L^2 = 0.26$ ;    —  $t x D/L^2 = 1.8$

Furthermore and surprisingly, the interfacial concentration and thus the tie-line for transformation is almost time-independent as shown in Figure 5.10. This can be explained by the fact that the pressure jump on both sides of the interface is almost time independent (see Figures 5.8). An alternative interpretation is to address issues related to the evolution of elastic strain energy in the system. It is clear from the work of Cahn and Larché [34] that elastic strain energy influences the compositions at the interface between the precipitate and the matrix. If it is assumed

that the atomic fraction of precipitates  $f_a^\beta$  is small, the molar Gibbs energy of precipitate is shifted by a quantity proportional to  $\frac{\partial G^{el}}{\partial f_a^\beta}$  where  $G^{el}$  is the volumetric elastic energy stored in the system due to the formation of  $\beta$ -precipitate in the  $\alpha$ -matrix [12]. This results from the idea that the Gibbs energy of a stressed system is obtained by adding an extra term to the Gibbs energy of the unstressed system [43]. In that case, in the same way as for the Gibbs-Thomson effect [44, 45], the elastic strain energy affect the interfacial concentration  $X_B^{\alpha/I}$  as follow :

$$X_{B,el}^{\alpha/I} = X_B^{\alpha/I} \exp\left(\frac{V^\beta}{RT} \frac{\partial G^{el}}{\partial f_a^\beta}\right) \quad (22) \text{ where } V^\beta \text{ is}$$

the molar volume of the precipitate. However, there is no simple analytical expression of  $G^{el}$  in the case of complex particle morphologies and anisotropic elastic properties. If one assumes that the elastic properties of both the matrix and the precipitate are similar and the atomic fraction of precipitates  $f_a^\beta$  is small, then Equation (22) can be reduced to [12]:

$$X_{B,el}^{\alpha/I} = X_B^{\alpha/I} \exp\left(\frac{V^\beta}{RT} \frac{G^{el}}{f_a^\beta}\right) \quad (23)$$

From our 3D calculations, it is possible to determine the elastic strain energy density. It is defined by the classical relation :

$$G^{el} = \frac{1}{V_t} \int_{V_t} \frac{1}{2} \boldsymbol{\varepsilon} : \boldsymbol{\sigma} dV$$

where  $\boldsymbol{\varepsilon}$  is the strain tensor,  $\boldsymbol{\sigma}$  is the stress tensor and  $V_t$  is the total volume of the system.

Our calculations show Figure 5.11 that the majority of elastic strain energy is concentrated in the minority phase which is here the precipitate. The elastic strain energy was thus calculated as a function of atomic fraction of precipitate in Table 3.

**Table 3:** Values of both elastic strain energy  $G^{el}$  and ratio  $\frac{G^{el}}{f_a^\beta}$  as a function of atomic fraction of precipitates

$f_a^\beta$ . The adimensional time ( $t \times D/L^2$ ) and radius ( $r/L$ ) are intended for information purposes.

$t \quad \square D/L^2$	$r/L$	$f_a^\beta$ (%)	$G^{el}$ (J/m <sup>3</sup> )	$\frac{G^{el}}{f_a^\beta}$ (J/m <sup>3</sup> )
0	0.05	$5.3 \cdot 10^{-2}$	13.54	2.55E+04
0.056	0.07	$1.5 \cdot 10^{-1}$	38.75	2.58E+04
0.15	0.092	$3.3 \cdot 10^{-1}$	88.6	2.71E+04
0.26	0.11	$5.6 \cdot 10^{-1}$	152.8	2.73E+04
0.4	0.127	$8.6 \cdot 10^{-1}$	236.1	2.75E+04
1.8	0.16	1.7	470.9	2.77E+04

Another lesson that we can learn from our calculations is that the ratio  $\frac{G^{el}}{f_a^\beta}$  does not depend on  $f_a^\beta$  and can be approximately considered as constant and equal to 26000 J/m<sup>3</sup>. This result, already observed in the case of both  $\gamma/\gamma'$  nickel-based super alloys and Si<sub>3</sub>N<sub>4</sub> precipitation in ferrite [12, 13], explain why the interfacial concentrations do not evolve significantly with time according to Equation (23).

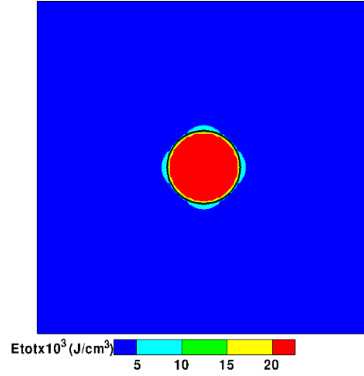


**Figure 5.11** : Elastic strain energy within the three equivalent middle plane  $x=0.5$ ,  $y=0.5$  and  $z=0.5$  at time  $t \times D/L^2 = 0.4$  of the growth process.

### 5. 3. Growth of a single spherical precipitate into a matrix under applied uniaxial compression loading

The effects of external pressure on the growth of spherical precipitate were also studied. The same cubic system containing the spherical particle of adimensional radius  $r/L=0.05$  is deformed through uniaxial compressive loading applied on the two opposite  $yz$ -cube faces (see Figure 5.12a). For Eulerian discretization, compression is simulated by injecting matrix at molar fraction  $x_A^\beta = 0.1$  and at constant velocity through the two  $yz$ -cube faces. The displacement field is constrained to periodic conditions at the four other system surfaces. The physical and dynamic constants are those given in table 1. The elastic constants are set different for the particle and the matrix in order to induce pressure gradient within the two-phase system (see Table 4). The Young's modulus of the particle is thus taken twice higher than that of the matrix ( $E_Y^\alpha = 2E_Y^\beta = 4.2 \times 10^{11}$  Pa). The compression loading is applied until an average pressure gap of 100 MPa between particle and matrix was reached.

**Table 4** : Elastic constants used for calculations

	Symbol	$\alpha$ -phase	$\beta$ -phase
Young's modulus (GPa)	$E_Y$	210	420
1 <sup>st</sup> Lamé's coefficient (GPa)	$\mu_E$	105	210
Isothermal compressibility coefficient (Pa <sup>-1</sup> )	$\chi_T$	$1.43 \times 10^{-11}$	$7.14 \times 10^{-12}$

In that case, calculations given in Figure 5.12 show that non-isotropic pressure gradient are induced within both equivalent the  $y=0.5$  and  $z=0.5$  planes while isotropic gradient are involved within the  $x=0.5$  plane. Also, a high-pressure gradient is involved along the  $(x; y=0.5, z=0.5)$ -line within the matrix in a relatively confined area around the particle; the level of pressure being larger that the distance to particle is smaller. Conversely, within the  $x=0.5$ -plane, pressure gradient is much lower with decreasing pressure feature when going towards the particle. As a consequence, a 3D elastic field anisotropy was induced by the applied stress. The calculation of the particle growth driven by the chemical/mechanical coupling of the diffusion process is subsequently performed in the framework of this non-isotropic stress field. The system is constrained to a constant volume during calculation and periodic boundary conditions are set at the six system surfaces.

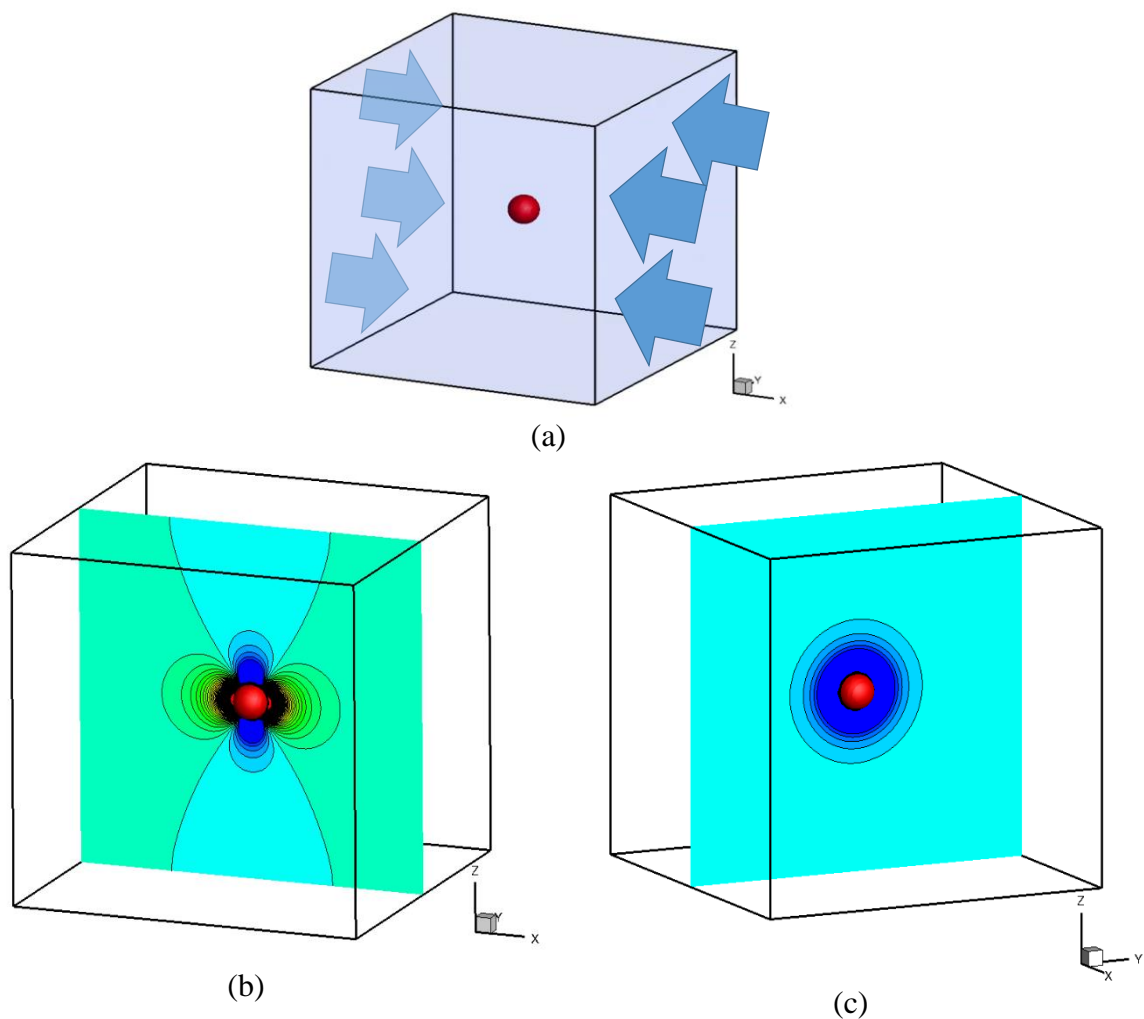


**Figure 5.12** : (a) The initial cube is deformed through uniaxial compressive loading applied on the two opposite  $yz$ -cube faces until an average pressure gap of  $10^8$  Pa between particle and matrix is reached. Pressure maps after compressive loading within (b) the  $y=0.5$ -plane (equivalent to the  $z=0.5$ -plane) and (c) the  $x=0.5$ -plane. The iso-pressure lines in the matrix evolves from  $2.75 \times 10^8$  Pa (dark blue) to  $3.5 \times 10^8$  Pa (red) with pressure step of  $0.01 \times 10^8$  Pa. Pressure in the particle reach  $4.2 \times 10^8$  Pa.

Surprisingly, a change in morphology is shown to occur during the particle growth as shown in Figure 5.13. Indeed, nearly from the beginning, the particle morphology deviates from the spherical shape (Figure 5.13b). The growth

is limited along the  $(x/L, y/L=0.5, z/L=0.5)$  line, while it is enhanced along the  $(x/L=0.5, y/L, z/L=0.5)$  and the  $(x/L=0.5, y/L=0.5, z/L)$  lines. This change in morphology is clearly not induced by the interactions between the diffusion fields and the free boundaries since it begins for low volume fraction of particles.

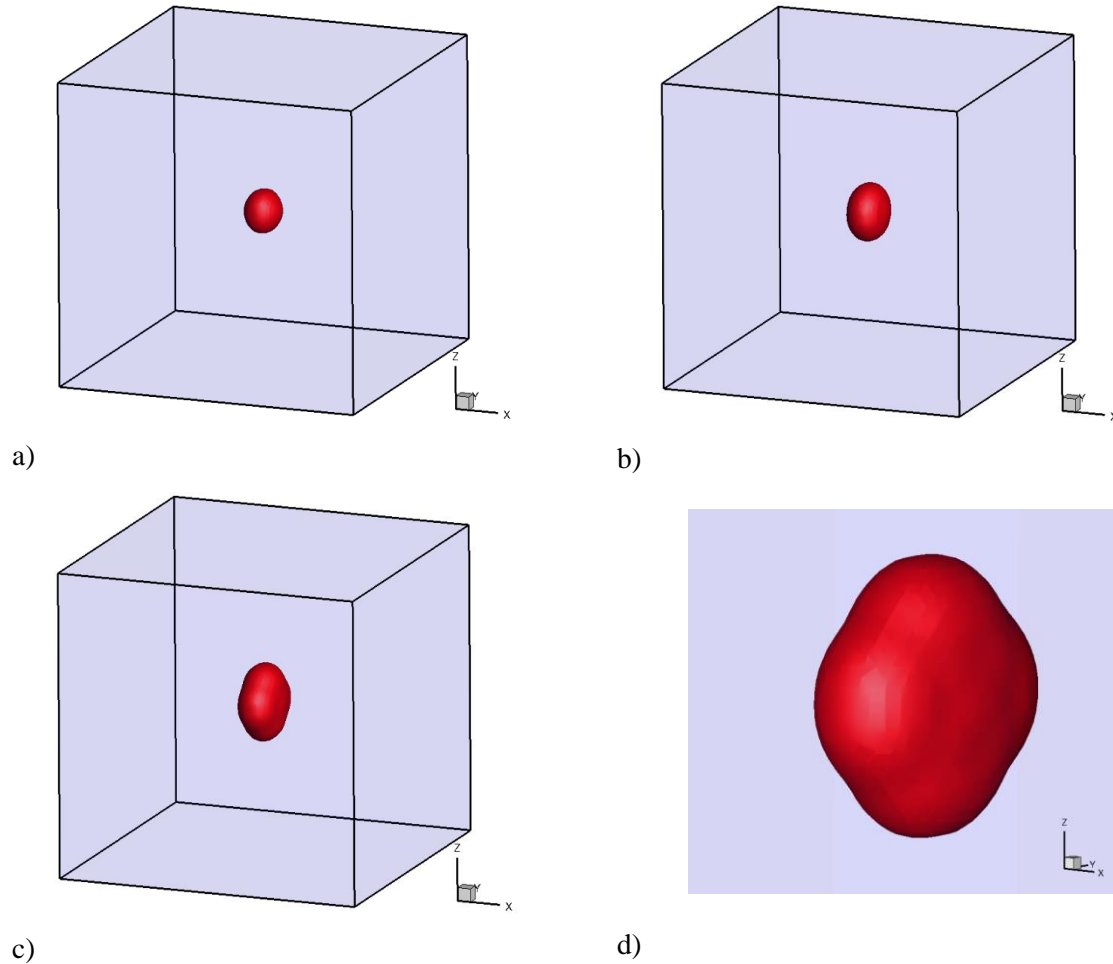


**Figure 5.13** :Non-isotropic evolution of the growth morphology of the initial spherical particle of adimensional radius  $r/L=0.05$  within the stress field induced by uniaxial compressive loading. (a)  $t \times D/L^2 = 0.15$  ; (b)  $t \times D/L^2 = 0.4$  ; (c) and (d)  $t \times D/L^2 = 1.85$

The time-evolution of the pressure and molar fraction within the  $y=0.5$  plane (or the equivalent  $z=0.5$  plane) during particle growth is given in Figure 5.14. As expected and contrary to the case of self-induced elastic fields, the stress field is no longer isotropic and uniform in the matrix. Furthermore, the interface concentration becomes function of local position in the presence of the applied stress as the system is elastically inhomogeneous. In the  $x$ -axis, the closer to the interface in the matrix side, the higher the pressure is, the lower the pressure jump at the interface is and thus the lower the composition is. The interface motion in that direction is shown to be slowed down for the reason that pressure and composition gradients are of opposite signs (see arrows in Figures 5.14 b) and e)). In the  $y$ -axis (or  $z$ -axis), the picture is somehow different since both gradients have the same sign. In that case, even if the concentration gradient is kinetically less favorable to particle growth compared to that along the  $x$ -axis, the pressure gradient is not opposed to the particle growth and kinetics is shown to be faster.

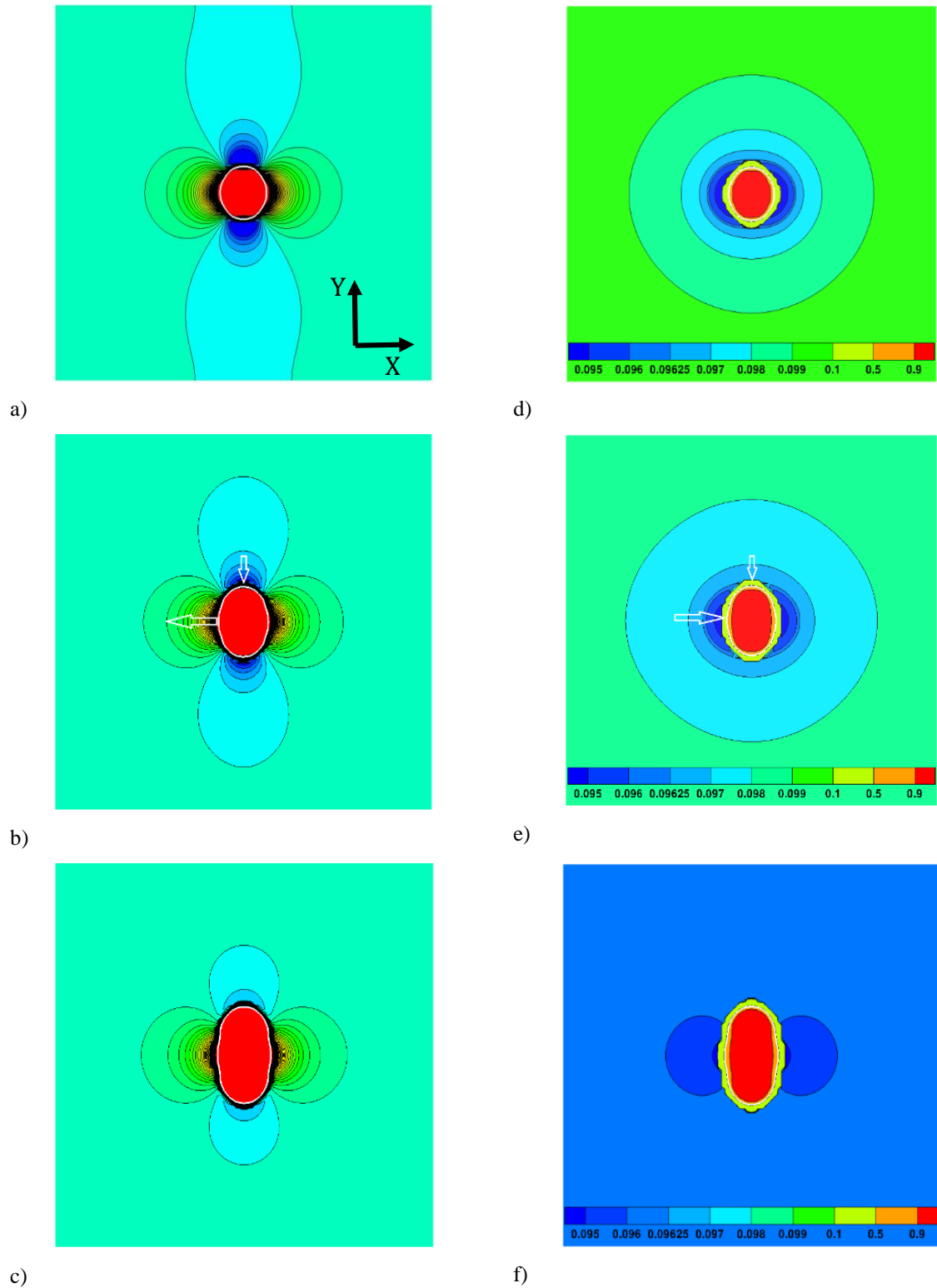


**Figure 5.14:** Pressure maps [(a), (b), (c)] and molar fraction maps of  $B$  [(d), (e), (f)] within the equivalent  $z=0.5$ -plane (or equivalent  $z=0.5$ -plane) at different times of the particle growth process: (a) and (d),  $t \times D/L^2 = 0.15$  ; (b) and (e),  $t \times D/L^2 = 0.4$  ; (c) and (f),  $t \times D/L^2 = 1.85$ . The iso-pressure lines evolve from  $2.75 \times 10^8$  Pa (dark blue) to  $3.5 \times 10^8$  Pa (red) with pressure step of  $0.01 \times 10^8$  Pa.

This is confirmed, Figure 5.15, by the calculations of kinetics of interface motion within the  $z=0.5$  plane and along both the  $x$ -axis and  $y$ -axis. Indeed, the kinetics of interface motion is clearly shown to be much more faster in  $y$ -axis. Also noteworthy is that the equilibrium position of the interface depends on the given direction.

Within  $x=0.5$  plane, both pressure and composition fields remain isotropic during most of the particle growth (Figure 5.16). In that case, as expected, the particle morphology remains circular in this plane. However, for longer time the elastic field is no longer isotropic in the vicinity of the particle (Figure 5.16 c)), and consequently the morphology deviates from a circle to a pseudo-square. In that case, it mainly results from the non-uniform interface composition shift induced by the non-uniform pressure jump at the interface, which contributes to slow the kinetic growth in the  $x=0.5$  plane diagonals. Finally, the applied field is shown to break the symmetry of the problem as already suggested in [46, 47]. It is worth noting that the morphology evolution and the kinetics are expected to depend on the elastic properties of both the precipitate and the matrix, the magnitude and the nature of the field applied [46, 47].

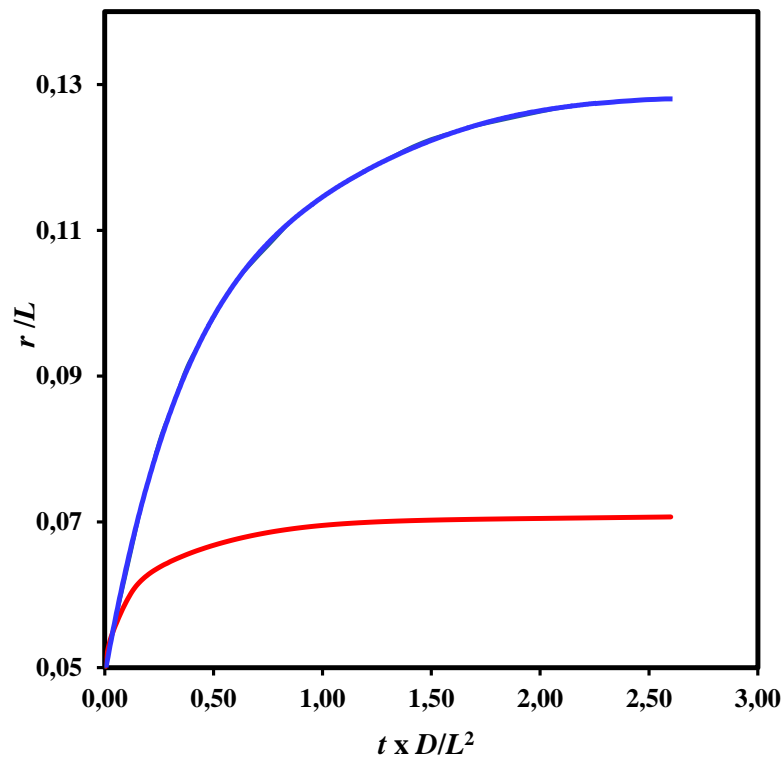


**Figure 5.15** : Kinetics of the particle growth within the stress field induced by the uniaxial compression perpendicular to the  $x=0$  plane. Geometry parameters are plotted within the plane ( $z=0.5$ ) in order to exhibit the growth anisotropy.

- half value of the particle width  $r_x/L$  along the  $(x/L, y/L=0.5, z/L=0.5)$ -line
- half value of the particle width  $r_y/L$  or  $r_z/L$  along the  $(x/L=0.5, y/L, z/L=0.5)$ -line or the  $(x/L=0.5, y/L=0.5, z/L)$ -line, respectively.

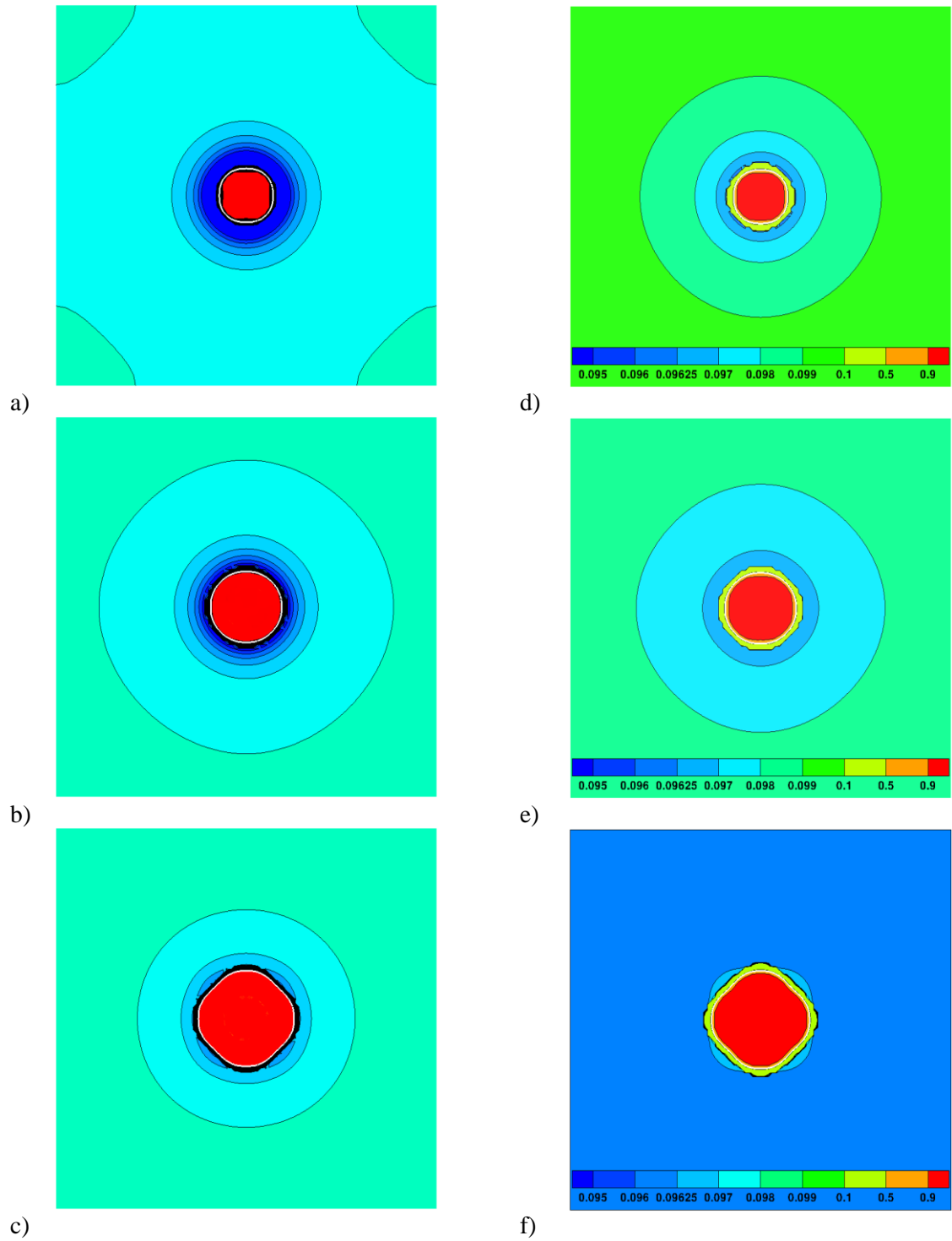


Figure 5.16 : Pressure maps [(a), (b), (c)] and molar fraction maps of the *B*-atoms [(d), (d), (f)] within the  $x=0.5$ -plane at different times of the particle growth process:  
 (a) and (d),  $t \times D/L^2 = 0.15$  ; (b) and (e),  $t \times D/L^2 = 0.4$  ; (c) and (f)  $t \times D/L^2 = 1.85$ .  
 The iso-pressure lines evolve from  $2.75 \times 10^8$  Pa (dark blue) to  $3.5 \times 10^8$  Pa (red) with pressure step of  $0.01 \times 10^8$  Pa.

## 6. CONCLUSION

A 3D model originally developed for fluid flow and elastic solid deformation was extended to the coupling between diffusive phase transformations and mechanic fields. This model is shown to be able to describe the time-evolution of both chemical and mechanic fields and their interactions in 3D complex geometries. It was applied successfully in order to analyse the effects of both internal and external stresses on the growth of an initially spherical precipitate embedded into a supersaturated matrix. The elastic effects are shown to affect the transformation kinetics, the equilibrium state and the morphological evolution. This 3D model that can be applied to multicomponent systems and to complex geometries offers new perspectives for a better understanding of the microstructure evolution in metallic alloys.

## REFERENCES

- [1] Q. Lai, L. Brassard, O. Bouaziz, M. Gouné, M. Verdier, G. Parry, A. Perlade, Y. Bréchet, T. Pardoen, *Int. J. Plasticity* 80 (2016) 187-203
- [2] Q. Lai, O. Bouaziz, M. Gouné, A. Perlade, Y. Bréchet, T. Pardoen, *Mater. Sci. Eng. A* 638 (2015) 78-89
- [3] E. Botcharova, J. Freudenberger, L. Schultz, *Acta Mater.* 54 (2006) 3333–3341
- [4] K. Kondo, T. Chiba, S. Yamada, *J. Magn. Mater.* 254–255 (2003) 541-543
- [5] J. W. Cahn, F. C. Larché, *Acta Metall.* 32 (1984) 1915-1923
- [6] R. O. Williams, *Calphad* 8(1) (1984) 1-14
- [7] W.C. Johnson, P.W. Voorhees, *Metall. Trans.* 18A (1987) 1213-1228
- [8] P. Jessner, M. Gouné, R. Danoix, B. Hannyoy, F. Danoix, *Philos. Mag. Lett.* 90 (2010) 793-800
- [9] F. C. Larché, J. W. Cahn, *Acta Metall.* 30 (1982) 1835
- [10] M. Doi, *Mat. Trans. JIM* 33 (1992) 637-649
- [11] T. Grosdidier, A. Hazotte, A. Simon, *Mater. Sci. Eng. A* 256 (1998) 183-196
- [12] H. Van Landeghem, M. Gouné, S. Bordère, F. Danoix, A. Redjaimia, *Acta Mater.* 93 (2015) 218-234
- [13] A. Hazote, T. Grosdidier, S. Denis, *Scripta Mater.* 34 (1996) 601-608
- [14] T. Eto, A. Sato, T. Mori, *Acta Metall.* 26 (1978) 499-508.
- [15] V. Perovic, G.R. Purdy, L.M. Brown, *Acta Metall.* 27 (1979) 1075-84.
- [16] W.C. Johnson, *Acta Metall.* 32 (1984) 465-75
- [17] J.K. Tien, R.P. Gamble, *Metall. Trans.* 3 (1972) 2157-2162.
- [18] O. Diard, S. Leclercq, G. Rousselier, G. Cailletaud, *Int. J. Plasticity* 21 (2005) 691-722

- [19] A. Musienko, A. Tatschl, K. Schmidegg, O. Kolednik, R. Pippan, G. Cailletaux, *Acta Mater.* 55 (2007) 4121-4136
- [20] A. Duga, P. Wollants, N. Moelans *Comput Mater. Sci.* 99 (2015) 81-95
- [21] Kais Ammar, Benoît Appolaire, Georges Cailletaud, Frederic Feyel, Samuel Forest, *Comput. Mater. Sci.* 45 (2009) 800–805
- [22] Kais Ammar, Benoît Appolaire, Georges Cailletaud, Samuel Forest, *Eur. J. Comput. Mech.* 18 (2009) 485-523
- [23] M. Cottura, B. Appolaire, A. Finel, Y. Le Bouar, *Acta Mater.* 72 (2014) 200-210
- [24] Shingyu Leung, Hongkai Zhao, *J. Comput. Phys.* 228 (2009) 2993–3024
- [25] J. Stefan, *Ann. Phys. Chem.* 42 (1891) 269–286.
- [26] L. Q. Chen, *Annu. Rev. Mater. Res.* 32 (2002) 113-140
- [27] S. Bordère S, J-P. Caltagirone, *J. Fluids. Struct.* 51 (2014) 344–353.
- [28] S. Bordère, J-P. Caltagirone, *Comput. Struct.* 164 (2016) 38-52.
- [29] R. Scardovelli, S. Zaleski, *Annu. Rev. Fluid. Mech.* 1999 31, 567–603.
- [30] R. Scardovelli, S. Zaleski, *Int. J. Numer. Meth. Fluids* 41 (2003) 251–274.
- [31] W. Aniszewski, T. Ménard, M. Marek, *Comput. Struct.* 97 (2014) 52–73.
- [32] J.C.M. Li, *Metall. Trans. A* 9 (1978) 1353-1380
- [33] J.C.M. Li, *Scr. Metall.* 15 (1981) 21-28
- [34] F. C. Larché, J. W. Cahn, *Acta Metall.* 26 (1978) 1579-1589
- [35] F. C. Larché, P. W. Voorhees, *Def. Diff. Forum* 129-130 (1996) 31-36
- [36] J-P. Caltagirone, *Discrete mechanics*. London: ISTE, John Wiley & Sons (2015)
- [37] H. Meier, J. Alves, M. Mori M, *Comput. Chem. Eng.* 23 (1999) 247–62
- [38] S. Vincent, J-P. Caltagirone, P. Lubin, T. N. Randrianarivelo TN, *Comput. Fluids* 33 (2004) 1273–1289
- [39] C. Zener, *J. Appl. Phys.* 20 (1949) 950–953.
- [40] G. W. Scherer, *Relaxation in glass and composites*, ed. Wiley 1986, re-ed Krieger Pub. (1992)
- [41] J. D. Eshelby, *Acta Metall.* 3 (1955) 487-490
- [42] V. J. Laraia, W. C. Johnson, *J. Mater. Res.* 3 (1988) 257-266
- [43] Z-K. Liu, J. Agren, *Acta Metall. Mater.* 38 (1990) 561–572.
- [44] P. Maugis, M. Gouné, *Acta Mater.* 53(2005) 3359–3367.
- [45] M. Perez, *Scripta Mater.* 52 (2005) 709-712
- [46] P. H. Leo, H-J. Jou, *Acta Metall. Mater.* 41 (1993) 2271-2281
- [47] W. C. Johnson, *Metall. Trans. A* 18A (1987) 233-247